PAPER

A dual-modal ROS generator based on multifunctional PDA–MnO₂@Ce6 nanozymes for synergistic chemo-photodynamic antibacterial therapy†

Anni Cui,[a] Ying Bao,[b] Haitao Xu,[c] Xin Mu,[a] Xiahua Zhong,[a] Wynn Wee,[b] Fanqi Wu[d] and Guiye Shan ⓘD *[a]

The rapid emergence of drug-resistant bacteria has attracted great attention to exploring advanced antibacterial methods. However, single-modal antibacterial therapy cannot easily eliminate drug-resistant bacteria completely due to its low efficacy. Therefore, it is essential to achieve multi-modal antibacterial therapy effectively. Herein, a dual-modal ROS generator was designed based on photosensitive PDA–MnO₂@Ce6/liposome (PMCL) nanozymes for synergistic chemo-photodynamic therapy. PMCL nanozymes adhere to bacteria through liposome–membrane fusion. Meanwhile, PMCL catalyzes endogenous hydrogen peroxide (H_2O_2) to generate hydroxyl radicals (˙OH) and singlet oxygen ($^1O_2$) under laser irradiation. Furthermore, the photothermal effect can accelerate the generation of ROS. Based on dual-enzyme activities (mimicking peroxidase and catalase) and photodynamic properties, PMCL achieves powerful antibacterial efficacy and mature bacterial biofilm eradication. With the synergistic chemo-photodynamic effects, bacterial populations decrease by >99.76% against Gram-positive *S. aureus* and Gram-negative *E. coli*. Notably, the synergistic antibacterial properties of PMCL nanozymes are further explored using a mouse wound model of *S. aureus* infection. This work fabricated an efficient dual-modal ROS generator to kill bacteria, further providing a new strategy for treating wound infection.

1. Introduction

Infections caused by pathogenic bacteria pose a serious threat to human health, inducing multiple diseases and complications.[1,2] Antibiotic drugs are generally a widely used strategy for combating bacteria.[3,4] However, the overuse of antibiotics causes the formation of multidrug-resistant bacteria.[5] Consequently, it is urgent to develop effective antibacterial strategies for eradicating bacteria. Due to no drug resistance and fewer side effects, photodynamic therapy (PDT) and chemodynamic therapy (CDT) have been focused on for antibacterial

[a]Centre for Advanced Optoelectronic Functional Materials Research, Key Laboratory for UV Light-Emitting Materials and Technology of the Ministry of Education, Northeast Normal University, Changchun, 130024, China.
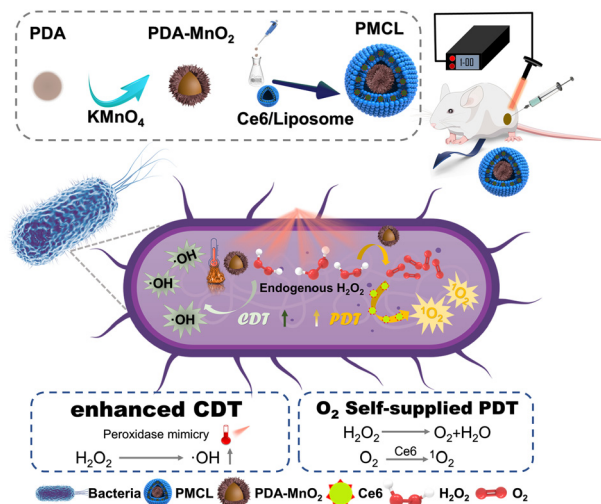*E-mail: shangy229@nenu.edu.cn*
[b]Department of Chemistry, Western Washington University, Bellingham, WA 98225, USA
[c]Department of Ophthalmology, the Second Hospital of Jilin University, Changchun 130041, China
[d]Department of General Science: Chemical Biology, Thompson Rivers University, Kamloops, BC V2C 0C8, Canada
†Electronic supplementary information (ESI) available. See DOI: https://doi.org/10.1039/d2bm01939f

treatment.[6–9] The generated singlet oxygen ($^1O_2$) by the photosensitizers can kill drug-resistant bacteria during the PDT process.[10,11] Highly toxic hydroxyl radicals (˙OH) cause bacterial protein and DNA damage during CDT.[12,13] However, PDT-mediated continuous O_2 depletion hinders the production of singlet oxygen ($^1O_2$) in the hypoxic environment.[14,15] CDT is limited by low catalytic efficiency.[16,17] Therefore, it is difficult to effectively eliminate bacteria by a single modal therapeutic strategy.[18] Thus, integrating a dual-modal antibacterial strategy is beneficial for overcoming the limitation of single therapy and improving the therapeutic efficiency.

Currently, the dual-modal ROS ($^1O_2$ and ˙OH) system is expected to achieve chemo-photodynamic therapy simultaneously.[19,20] MnO₂ as a catalase creates sufficient oxygen by decomposing H_2O_2, which promotes $^1O_2$ generation for enhancing PDT.[21,22] Meanwhile, MnO₂ as a peroxidase-like nanozyme catalyzes endogenous H_2O_2 to produce ˙OH for chemodynamic treatment.[23,24] However, the catalytic activity of MnO₂ nanozymes is generally limited.[25] Therefore, it is crucial to improve the catalytic properties of MnO₂ nanozymes. Polydopamine (PDA) has an extended π-conjugated electron system, exhibiting high mobility of charge carriers and excellent photothermal conversion efficiency.[26,27] The amino and

Scheme 1 Schematic illustration of the PMCL nanozymes applied for synergistic chemo-photodynamic bacteria-infected wound therapy.

catechol groups in PDA have a strong binding ability towards nanomaterials.[28,29] Besides, the catalytic efficiency is further improved by the photothermal effect.[30] Therefore, the combination of PDA and MnO_2 can enhance the catalytic activity effectively. In addition, extracellular polymeric substances (EPS) of bacterial biofilms prevent antibacterial materials reaching the interior.[31,32] Liposomes can adhere to the bacterial membrane and deliver antibacterial materials to the bacteria.[33,34] Therefore, it is necessary to integrate PDA, MnO_2, the photosensitizer and liposomes together for achieving chemo-photodynamic therapy.

Herein, a dual-modal ROS generator based on PDA–MnO_2@Ce6/liposome (PMCL) nanozymes is prepared for treating bacterial infections by synergistic chemo-photodynamic therapy. The fabrication and antibacterial mechanism of PMCL nanozymes are shown in Scheme 1. PMCL nanozymes can adhere to bacteria through liposome–membrane fusion. MnO_2 continuously catalyzes endogenous H_2O_2 for generating ·OH and O_2. Then, Ce6 molecules encapsulated in liposomes utilize sufficient oxygen to generate singlet oxygen ($^1O_2$) for enhancing the PDT effect. The photothermal effect of PDA is used to further improve ·OH generation in the CDT process. Therefore, PMCL nanozymes as dual-modal ROS generators enhance the efficiency of PDT and CDT, respectively. Thus, PMCL can promote the generation of multiple ROS to inhibit the formation of bacterial biofilms. The PMCL nanozymes can kill bacteria effectively and can be applied for the treatment of wound infection in mice successfully.

2. Experimental section

2.1. Materials

Dopamine hydrochloride and hydroxymethyl aminomethane (Tris) were purchased from Sinopharm Chemical Reagent (Beijing, China). Potassium permanganate ($KMnO_4$), lecithin, cholesterol, hydrogen peroxide (H_2O_2), and chloroform ($CHCl_3$) were purchased from Beijing Chemical Works. Ce6 was purchased from J&K Scientific (Beijing, China). 2,2,6,6-Tetramethyl-piperidin (TEMP) and 1,3-diphenyl-2-benzofuran (DPBF) were obtained from Aladdin Industrial Corporation. The SYTO/PI double staining kit was purchased from Macklin Co., Ltd (Shanghai, China). *Staphylococcus aureus* (*S. aureus*, ATCC 29213) and *Escherichia coli* (*E. coli*, ATCC 25922) were obtained from AiYan Technology Co., Ltd (Shanghai, China).

2.2. Instruments

The morphology and composition of the samples were analyzed using a JEM-2010 transmission electron microscope (TEM) equipped with an energy dispersive X-ray (EDX) spectroscopy system. The X-ray diffraction (XRD) patterns were obtained using a Rigaku D/max-2500 XRD (Rigaku, Japan). The UV-vis absorption spectra were recorded using a UH4150 spectrophotometer (Hitachi High-Tech Science Corporation, Japan). The surface functional chemical groups were tested by Fourier transform infrared (FTIR) analysis (FTIR Systems Inc., USA). Electron spin resonance (ESR) spectra were measured using a Bruker EMXnano electron paramagnetic resonance spectrometer (Billerica, USA).

2.3. Preparation of PMCL nanozymes

The PDA nanoparticles were prepared by a hydrothermal method. First, a water–ethanol system was prepared by mixing 18 mL H_2O and 8 mL C_2H_5OH in a beaker. Then, Tris-HCl solution was added to the water–ethanol system under stirring for 20 min. Next, dopamine hydrochloride (150 mg) was added to the above mixed solution under stirring for 12 h. The PDA nanoparticles were washed three times with water and two times with ethanol, and dried at room temperature. Then, 15 mg of the obtained dry PDA was re-dispersed in 2.5 mL of $KMnO_4$ solution (1.0 mg mL^{-1}). The mixed solution was stirred vigorously for 4 h. Finally, PDA–MnO_2 was washed with deionized water and ethanol several times, respectively, to remove impurities and vacuum dried. A mixture of lecithin, cholesterol, and Ce6 at a molar ratio of 5 : 2 : 0.5 was dissolved in 4 mL of $CHCl_3$, and then air-dried under nitrogen. Afterwards, 4 mL of deionized water was added and sonicated for 10 min to peel off the dried membrane. Then, 1 mL of PDA–MnO_2 solution (0.3 mg mL^{-1}) was added to the above solution and stirred for 30 min to finally obtain PMCL nanozymes. The PMCL nanozymes were successively extruded 15 times using a 200 nm polycarbonate filter. Next, the filtered solution was centrifuged (25 min, 8000 r) and washed 5 times to eliminate free Ce6 and PDA–MnO_2. PDA/liposome (PL) was prepared using a similar method to that of PMCL without Ce6 and MnO_2. In the same way, PDA@Ce6/liposome (PCL) and PDA–MnO_2/liposome (PML) were prepared.

2.4. Photothermal properties of PMCL nanozymes

The photothermal performance was analyzed by irradiating a quartz cuvette containing aqueous dispersion of PMCL at

different concentrations (0.2, 0.4, 0.6, 0.8 and 1.0 mg mL^{-1}) using a 671 nm laser (1.5 W cm^{-2}, 10 min). Upon setting deionized water as the control group, PMCL aqueous solution was irradiated for 25 min, and then cooled down naturally. Furthermore, to explore the laser power density effect on the photothermal performance, 1.0 mg mL^{-1} PMCL solutions were exposed to the laser at different powers (0.6, 0.8, 1.0 and 1.5 W cm^{-2}). The temperature of the aqueous dispersion was measured and recorded using an infrared camera.

2.5. Peroxidase-like properties of PMCL nanozymes

To investigate the peroxidase-like reaction properties of PMCL, 3,3′,5,5′-tetramethylbenzidine (TMB) as the ˙OH indicator was catalytically oxidized by H_2O_2. The TMB aqueous solution (30 μL, 1 mM), H_2O_2 (20 μL, 1 mM) solution, PMCL (30 μL, 5 μg mL^{-1}) and sodium dihydrogen phosphate (NaH$_2$PO$_4$, 120 μL, pH = 4.5) were added into the cuvette; the variation of absorption at 652 nm was recorded based on the UV-vis spectra.

2.6. O$_2$ and ROS generation of PMCL nanozymes

The capability of PMCL to generate O_2 from H_2O_2 was evaluated by measuring the amount of dissolved oxygen using a portable dissolved oxygen meter. PMCL of different concentrations (0, 5, 10 and 15 μg mL^{-1}) were dispersed into H_2O_2 solution (4 mM, pH = 6.8) and the amount of produced O_2 was recorded for 10 min. The $^1O_2$ generated by Ce6 under light irradiation (671 nm, 0.48 W cm^{-2}) was measured using a DPBF probe. DPBF solution (15 μg mL^{-1}) was added with Ce6, PMCL and PMCL + H_2O_2, respectively. Next, a UV-vis spectrometer was used for DPBF analysis. For ESR measurements, 100 μL of the aqueous solution of PMCL + H_2O_2, PMCL, Ce6 and H_2O were mixed with 500 μL of TEMP (50 mM) solution, respectively. After being irradiated under a 671 nm laser for 5 min, the mixture was characterized using a spectrometer. The ˙OH detection was also performed as described above, except for the irradiation and the use of DMPO (50 mM) as the spin-trapping agent.

2.7. Cytotoxicity evaluation

The *in vitro* cytotoxicity was evaluated by MTT assays. L929 cells (mouse fibroblast cell line) were chosen to evaluate the *in vitro* cytotoxicity of PMCL. The L929 cells were seeded in 96-well plates for 24 h (10^4 cells per well, 100 μL of medium). Then, the culture medium was discarded and incubated with different concentrations of PL, PCL, PML and PMCL (1, 2, 5, 10, 15, 20, and 30 μg mL^{-1}) for 24 h, respectively. The control group was established using PBS. Next, the L929 cells were washed twice with PBS. Fresh culture medium containing MTT was added to each well and incubated for another 4 h. The phototoxicity of the irradiation groups was evaluated similarly to the above procedure. 671 nm laser irradiation was applied after L929 cells were co-cultured with different concentrations of PL, PCL, PML and PMCL (1, 2, 5, 10, 15, 20, and 30 μg mL^{-1}). Finally, the mixture in each well was poured out and

replaced by 150 μL DMSO for determining the cell toxicity using a microplate reader.

2.8. Bacterial culture

E. coli (ATCC 25922) and *S. aureus* (ATCC 29213) were used in this study. The bacteria were grown in Luria–Bertani (LB) medium (37 °C, 12 h) and collected by centrifugation. Then, the bacteria were further scattered in PBS solution to adjust the content of 10^6 colony forming units (CFU) per milliliter. The bacterial dispersion was washed with saline and quantitated using a microplate reader.

2.9. Antibacterial and antibiofilm efficacy of PMCL nanozymes

Bacteria suspensions (500 μL, 1 × 10^6 CFU mL^{-1}) were co-incubated with PL, PML, PCL and PMCL nanozymes in a 96-well plate (37 °C, 2 h). Then the bacterial suspensions were treated by irradiation with a 671 nm laser (0.48 W cm^{-2}) or without laser, respectively. After each treatment, the bacterial suspensions were serially diluted with sterilized PBS. Then, 20 μL aliquot of the diluted solutions was spread on the LB agar. The standard plate count method was used to determine the number of viable bacteria. To evaluate the eradication effects of PMCL on bacterial biofilms, five groups were formed: (I) PBS, (II) PL, (III) PCL, (IV) PML and (V) PMCL. After being co-incubated for 12 h, the bacterial biofilms in the laser treatment groups were irradiated with a 671 nm laser (0.48 W cm^{-2}). Then, the biofilms in each group were rinsed with 0.9% physiological saline twice to remove the samples and floating bacteria. Subsequently, crystal violet (0.1%, 10 min) solution was added to each well to stain the biofilms for 30 min. The stained biofilms in each group were rinsed with 0.01 M PBS twice and dried at room temperature. Finally, the OD$_{600}$ values of the biofilms in each group were measured by UV-vis spectroscopy.

2.10. Intracellular ROS detection

The intracellular ROS production was investigated using DCFH-DA as an indicator. After bacterial uptake, DCFH-DA was deacetylated to non-fluorescent DCFH, which was later oxidized by ROS into fluorescent DCF. Briefly, the bacteria were cultured for 24 h at 37 °C, followed by treatment with PBS, PML, PCL and PMCL under laser irradiation (0.48 W cm^{-2}, 10 min). Then, the bacteria were co-incubated with DCFH-DA (10 μg mL^{-1}) for 20 min after rinsing with PBS. For the CLSM imaging study, the excitation wavelength was 488 nm and the emission wavelength was 550 nm. Finally, the fluorescence signals of the produced DCF were observed using confocal microscopy and further analyzed quantitatively.

2.11. Live/dead staining and morphological characterization

The fluorescence tagging method was used to detect the survival (live/dead) of the bacteria. Five groups were set up: PBS, PL, PML, PCL and PMCL. The bacterial biofilms were treated with PMCL nanozymes (20 μg mL^{-1}) for 30 min. The mixture with 671 nm laser irradiation (0.48 W cm^{-2}, 15 min) was collected

by centrifugation (5000 r, 10 min). Then, the treated biofilms were stained by incubating in a staining reagent containing 1 μM SYTO and 1 μM PI for 20 min in the dark. The adhesion between the biofilms and the materials was observed by CLSM using an oil-immersed ×100 objective lens. For the morphological observation, different groups of the bacterial suspensions were dropped on silicon slides and then fixed using 2.5% glutaraldehyde at 4 °C overnight. The fixed samples were gradually dehydrated with 20, 30, 50, 70, 80, 95, and 100% C_2H_5OH for 5 min. Finally, the samples were dried in air and observed by SEM.

2.12. *In vivo* therapy of *S. aureus*-infected wounds

All the animal experiments were approved by the Animal Care Committee of Jilin University and conformed to the Animal Ethical Standards and Use Committee at Jilin University. For the *in vivo* anti-infection assay, female BALB/c mice (6–8 weeks, body weight: ≈20 g) were purchased from Vital River Company in Beijing. The wounds ($d \approx 10$ mm) were made by surgical procedures on the back of the mice after anesthesia. Then, 200 μL of the bacterial suspensions (*S. aureus*, OD_{600} = 0.2) were used to infect the wounds. A total of 15 model mice infected with *S. aureus* were divided into five groups randomly. Subsequently, the groups (I) PBS (200 μL), (II) PL (200 μL; PDA: 2 mg kg^{-1}), (III) PCL (200 μL; PDA: 2 mg kg^{-1}; Ce6: 4 mg kg^{-1}), (IV) PML (200 μL; PDA: 2 mg kg^{-1}, MnO_2: 5 mg kg^{-1}) and (V) PMCL (200 μL; PDA: 2 mg kg^{-1}; Ce6: 4 mg kg^{-1}; MnO_2: 5 mg kg^{-1}) were subcutaneously injected into the infected wound on the first and fourth day, respectively. For the group that required laser irradiation, the wound site of the mice was exposed to a 671 nm laser (0.48 W cm^{-2}, 15 min) after administration. The initial day was identified as day 0, and the wound areas were imaged every 2 days. Then the suspensions were diluted and spread on LB-agar plates. After 18 h of co-incubation at 37 °C, the bacterial plaques on the plate were counted.

2.13. Statistical analysis

All the quantitative data in each experiment were evaluated and analyzed by one-way or two-way analysis of variance and expressed as the mean values ± standard deviations (SD). Data were presented as SD of a minimum of 3 samples ($n \geq 3$).

3. Results and discussion

3.1. Characterization of the PMCL nanozymes

PMCL nanozymes were prepared using a thin lipid film hydration method. For PMCL nanozymes, Ce6 was wrapped in the hydrophobic layer and PDA–MnO_2 was encapsulated in a hydrophilic cavity. The SEM image of PDA nanoparticles shows a uniform size of about 122 nm (Fig. 1A). The morphology and structure of PDA–MnO_2 based on the redox reaction between PDA and $KMnO_4$ are shown in Fig. 1B. The results show that rough MnO_2 structures are formed on the surface of PDA. Furthermore, the elemental mapping images
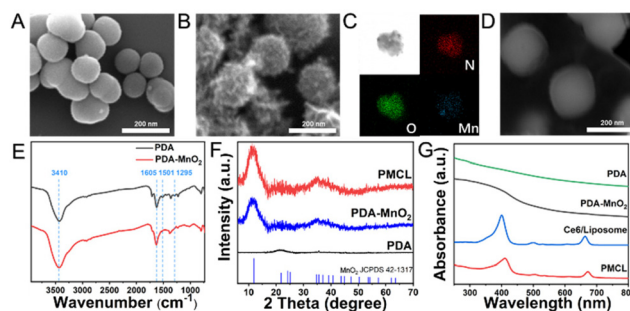

Fig. 1 SEM images of (A) PDA and (B) PDA–MnO_2. (C) TEM images and the EDX elemental mapping of PDA–MnO_2. (D) The SEM image of PMCL. (E) FT-IR spectra of PDA and PDA–MnO_2. (F) XRD spectra of PDA, PDA–MnO_2 and PMCL. (G) UV-vis absorption spectra of PDA, PDA–MnO_2, Ce6/liposome and PMCL.

illustrate the presence and homogeneous distribution of N, O, and Mn in PDA–MnO_2 (Fig. 1C). After coating with the liposome, the obtained PMCL nanozymes were close to spherical in shape with 180 ± 5.76 nm diameter. It is observed that the PMCL surface is covered with an organic film-like structure (Fig. 1D). The results were consistent with the hydrodynamic diameter measured by dynamic light scattering (Fig. S1†). The synthesized PDA–MnO_2 was further characterized by the XRD and FTIR spectra. As shown in the FTIR spectra (Fig. 1E), PDA shows four obvious characteristic bands at 1501 cm^{-1}, 3410 cm^{-1}, 1605 cm^{-1} and 1295 cm^{-1}, attributed to the N–H bending vibration, and the stretching vibrations of –OH, the benzene ring and the C–O bond, respectively. Compared with PDA alone, the FTIR spectrum of PDA–MnO_2 does not show the stretching vibration of the amine group at 1510 cm^{-1}, which is due to the formation of MnO_2 on the surface of PDA. The XRD spectra of PDA, PDA–MnO_2 and PMCL are shown in Fig. 1F. The results suggest that the characteristic peaks of PDA–MnO_2 appear at 12°, 24° and 37°, corresponding to standard birnessite MnO_2 (JCPDS 42-1317). It is observed that the crystal structure of PMCL is similar to that of PDA–MnO_2. The typical UV-vis absorption peaks of PDA–MnO_2 and Ce6/liposome may be detected at around 400 and 660 nm (Fig. 1G). The UV-vis absorption spectrum intensity of PMCL nanozymes was almost similar to that of Ce6/liposome, suggesting that the encapsulation of the liposome shows little change in the absorption properties.

3.2. Photodynamic activity of the PMCL nanozymes

Oxygen is an essential requirement during the process of PDT. For overcoming the hypoxic microenvironments of the biofilms, an efficient conversion of abundant endogenous H_2O_2 to O_2 is crucial for oxygen self-supply during the photodynamic process. Herein, the capacity for O_2 self-supply is assessed for the PMCL group through decomposing H_2O_2 (pH = 6.8). The pure H_2O_2 group was chosen as the control group. As shown in Fig. 2A, the PCL + H_2O_2 group and the H_2O_2 group produce almost no oxygen. However, for the PMCL + H_2O_2 group, the O_2 concentration reached 16.3 mg ml^{-1} in
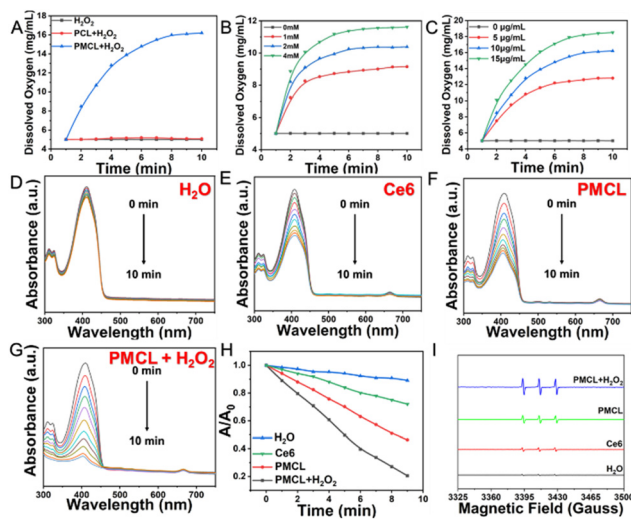
Fig. 2 (A) The O_2 content variation in different solutions (H_2O_2, PCL + H_2O_2 and PMCL + H_2O_2). (B) O_2 generation at different concentrations of H_2O_2 solution with PMCL (15 μg mL^{-1}). (C) O_2 generation at different concentrations of PMCL solution with H_2O_2 (4 mM). (D–G) The UV-vis absorption spectra of DPBF at different concentrations (H_2O, Ce6, PMCL and PMCL + H_2O_2) under laser irradiation (671 nm, 10 min). (H) DPBF absorption decay curves at 410 nm after laser irradiation (671 nm, 0.48 W cm^{-2}). (I) The ESR spectra of PMCL + H_2O_2, PMCL, Ce6 and H_2O.

10 min, indicating that MnO_2 as a catalase was the key element for the decomposition of H_2O_2 to produce O_2. Subsequently, the influence of different factors on the O_2 concentration was determined, as shown in Fig. 2B and C. The O_2 concentration was linearly related to the PMCL and H_2O_2 contents, respectively. Based on the above results, PMCL as a reliable O_2 self-supplied carrier can efficiently convert H_2O_2 to O_2. Furthermore, singlet oxygen was generated through O_2 molecules utilizing photosensitizers. The increased O_2 concentration may promote the rate of $^1O_2$ formation, thereby enhancing the PDT effect. To evaluate the $^1O_2$ generating capacity, DPBF served as an $^1O_2$ trapping reagent. The DPBF degradation rate was measured for the different groups including pure H_2O, Ce6, PMCL and PMCL + H_2O_2 as shown in Fig. 2(D–G). The formed $^1O_2$ may reduce the absorption peak intensity of DPBF at 410 nm. For the H_2O group, the absorption peak intensity of DPBF changed little under laser irradiation in 10 min. The results indicated that little singlet oxygen was formed. For the free Ce6 group (Fig. 2E) and PMCL group (Fig. 2F), the absorption peak intensity of DPBF showed an obvious decrease under 671 nm irradiation. In particular, the degradation of DPBF was evident for the PMCL + H_2O_2 group (Fig. 2G). The degradation rate of DPBF for the PMCL group and PMCL + H_2O_2 group was 55% and 82%, respectively (Fig. 2H). The above results suggested that the PMCL nanozymes based on O_2 self-supply lead to efficient $^1O_2$ production under 671 nm irradiation. Furthermore, the ESR spectra were explored to confirm the $^1O_2$ generation using TEMP as the spin-trapping reagent for the Ce6 group, PMCL group and PMCL + H_2O_2 group. The ESR spectra showed the triplet signal

$(1:1:1)$ of $^1O_2$, as shown in Fig. 2I. The ESR signal intensity of the PMCL + H_2O_2 group was the strongest, confirming that PMCL promotes the generation of more $^1O_2$. Therefore, PMCL nanozymes can be used as an effective oxygen self-supply agent for enhancing PDT in hypoxic bacterial environments.

### 3.3. Peroxidase-like properties of the PMCL nanozymes

The peroxidase-like activities of the PMCL nanozymes were investigated by the oxidation of 3,3′,5,5′-tetramethylbenzidine (TMB) in the presence of H_2O_2 (Fig. 3A). The hydroxyl radical is capable of oxidizing colorless TMB into blue-colored oxidized TMB (oxTMB), which can be quantitatively analyzed by UV-vis spectra (Fig. 3B). Only a low absorbance intensity was observed in the TMB + H_2O_2 and H_2O_2 groups. However, the TMB + H_2O_2 + PMCL group showed a high absorbance intensity at the wavelength of 652 nm. The results showed that PMCL exhibits peroxidase-like activity. To confirm the type of ROS, the ESR spectrum was measured using DMPO as the trapping agent. The characteristic ·OH signal $(1:2:2:1)$ was observed, indicating that PMCL can catalyze H_2O_2 to generate ·OH (Fig. S2†). The peroxidase-like activity of PMCL was further investigated using the H_2O_2 and TMB chromogenic system-based kinetic assay (Fig. 3C–F). The kinetic analysis results showed that PMCL exhibits a very low KM for both H_2O_2 ($K_M = 0.48$) and TMB ($K_M = 0.16$), indicating its extremely high affinity to the substrates. Thus, the prepared PMCL exhibits high peroxidase-like activity and catalyzes H_2O_2 to generate ·OH effectively.

3.4. Photothermal properties of the PMCL nanozymes

The photothermal performance of the PMCL nanozymes was systematically assessed. PDA exhibits an obvious photothermal effect. As shown in Fig. 4A, the increased temperatures were 47.8 and 49.2 °C for PCL and PMCL under laser irradiation (1.5 W cm^{-2}, 671 nm, 25 min), respectively. Besides, the heating curve of these groups was distinctly consistent with the photothermal images. MnO_2 cannot affect the photother-
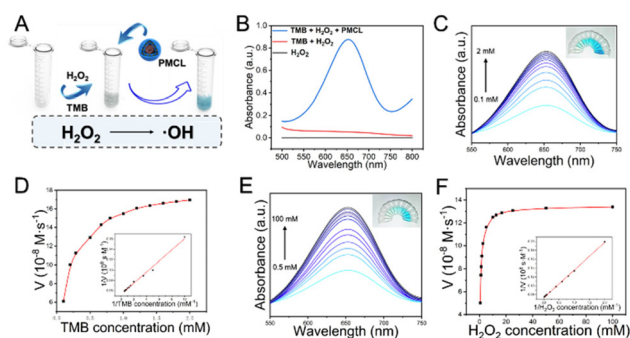
Fig. 3 (A) Schematic illustration of the enzymatic reaction accelerating the catalytic decomposition of H_2O_2 to produce ROS. (B) UV-vis spectra of TMB solutions with H_2O_2 under different conditions. TMB absorbance changes at 652 nm at different TMB concentrations (C) and H_2O_2 concentrations (E). Kinetic assay for the peroxidase-like activity of PMCL with H_2O_2 (D) and TMB (F) as the substrate.
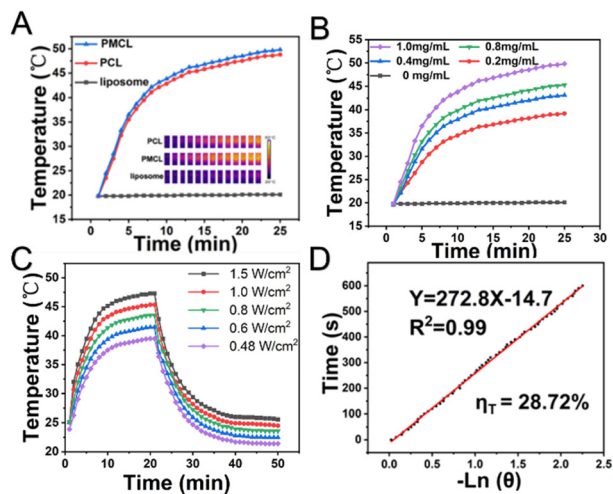
Fig. 4 Photothermal properties of the PMCL nanozymes. (A) Photothermal curves of the liposome, PCL, and PMCL (1.0 mg mL^{-1}) under laser irradiation (inset: the corresponding infrared (IR) thermal image of the liposome, PCL, and PMCL nanozymes under irradiation of a 671 nm laser). (B) Concentration-dependent temperature change curves of the PMCL nanozymes under laser irradiation (0.48 W cm^{-2}). (C) Temperature change of the PMCL nanozymes (0.2 mg mL^{-1}) with laser irradiation (0.48, 0.6, 0.8, 1.0 and 1.5 W cm^{-2}). (D) Calculation of the photothermal-conversion efficiency (η) of PMCL at 671 nm.

mal stability of PDA. To confirm the photothermal effect with different concentrations of PMCL, the temperature curves were collected at different time intervals under laser irradiation. As shown in Fig. 4B, the temperature increased monotonically with the PMCL concentration (0, 0.2, 0.4, 0.8 and 1.0 mg mL^{-1}). Additionally, the change of temperature presented a power-density-dependent photothermal performance (Fig. 4C). The photothermal-related local high temperature may destroy the healthy tissue. Therefore, we chose low-power laser irradiation (0.48 W cm^{-2}) to produce low-temperature PTT (<40 °C). Based on the heating–cooling curve and the corresponding thermal time constant (τ_s) (Fig. 4D), the photothermal conversion efficiency (η) of PMCL (1.0 mg mL^{-1}) was calculated to be 28.72%.

### 3.5. Photothermal-enhanced peroxidase-like activity of PMCL

According to the Arrhenius formula, nanozymes with near infrared absorption can efficiently convert light energy to heat energy, accelerating the catalytic reaction. Therefore, the introduction of a laser may promote the peroxidase-like activity of PMCL nanozymes. TMB molecules were chosen to detect the generated ˙OH. As shown in Fig. 5A, the mixed solution of TMB, H$_2$O$_2$ and PMCL showed an absorbance intensity at the wavelength of 652 nm. After 671 nm laser irradiation, the peroxidase-like activity of PMCL was significantly enhanced. In addition, the peroxidase-like activity of PMCL showed time-dependence under laser irradiation (Fig. 5B). Therefore, PMCL nanozymes showed better catalytic activity by generating more ˙OH under laser irradiation.
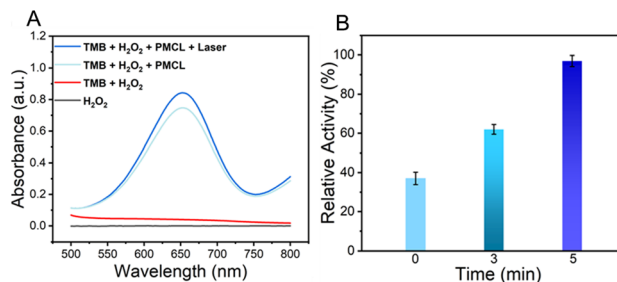
Fig. 5 (A) UV-vis spectra of TMB solutions with H$_2$O$_2$ under different conditions (H$_2$O$_2$, TMB + H$_2$O$_2$, TMB + H$_2$O$_2$ + PMCL and TMB + H$_2$O$_2$ + PMCL + laser). (B) The relative peroxidase-like activity of PMCL at different time points after laser irradiation.

3.6. *In vitro* antibacterial assay of the PMCL nanozymes

Due to the excellent chemo-photodynamic properties of the PMCL nanozymes, the antibacterial efficacy was evaluated by counting the number of colonies. To confirm the effect of the chemodynamic and photodynamic processes on the antibacterial performance, bacteria including *E. coli* (ATCC 25922) and *S. aureus* (ATCC 29213) were firstly treated with PL, PCL and PML, respectively (Fig. 6A). Without laser irradiation, the number of *E. coli* colonies for the PML group was obviously decreased and the bacterial inactivation reached 61.37%. Compared with the PL and PCL groups, the PML group showed an obvious antibacterial effect. This result was due to endogenous H$_2$O$_2$ being able to generate ˙OH catalysed by the peroxidase-like nanozymes. In contrast, compared with the control group, the number of colonies showed no significant change for the PL and PCL groups. After 671 nm laser irradiation, the number of colonies was decreased for the PL group due to the photothermal effect. Compared with the PL group, the PCL + laser group presented an evident decrease of the number of *E. coli* colonies due to the photodynamic effect. Moreover, the PML + laser group showed a significant reduction in the number of bacterial colonies based on the
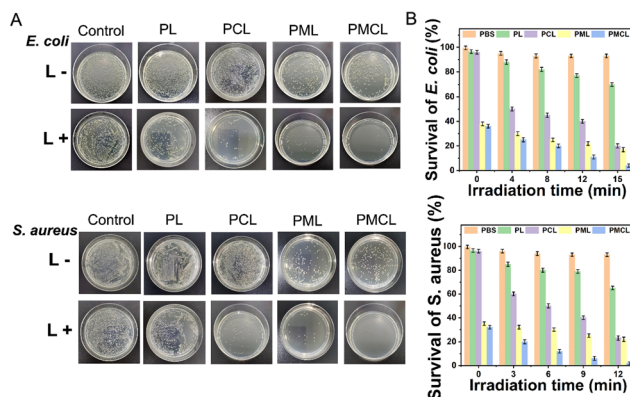
Fig. 6 (A) *E. coli* and *S. aureus* colonies on Luria−Bertani agar plates after treatments (PL, PCL, PML and PMCL) with and without light irradiation. (B) Relative bacterial viability of *E. coli* and *S. aureus* after treatments (PL, PCL, PML, PMCL) under different laser irradiation time, respectively.

chemodynamic effect. PMCL nanozymes can integrate the chemo-photodynamic effect to generate dual-modal ROS simultaneously. For the PMCL + laser group, the number of *E. coli* colonies decreased greatly, showing excellent synergistic bacteria killing effect. The percentage of bacterial survival under different laser irradiation time was evaluated (Fig. 6B). The bactericidal efficiency of the PMCL + laser group combating *E. coli* and *S. aureus* was 99.47% and 99.76%, respectively. Moreover, bacterial growth was further significantly retarded with laser irradiation (Fig. S3†).

To further verify the above experimental results, the stained images of live and dead bacteria were observed by live/dead staining assay. Two organic dyes (SYTO/PI) were introduced to distinguish the live and dead bacteria simultaneously. The live bacteria with intact membranes were labeled green, while the dead bacteria with damaged membranes were labeled red. As shown in Fig. 7A, compared with the PBS group (only green fluorescence was observed), all bacteria underwent a certain degree of damage after the treatment (PL, PCL, PML and PMCL). For the PL + laser group, only a few red fluorescence signals could be seen due to the weak photothermal effect under 671 nm laser irradiation. For the PML + laser and PCL + laser groups, the number of dead bacteria dramatically increased due to the generation of highly toxic $^{\bullet}OH$ and $^{1}O_2$, respectively. However, the single antibacterial mode can lead to incomplete sterilization. Therefore, PMCL nanozymes under the integration of the dual-modal ROS process showed red fluorescence signals brighter than any other groups. The above live/dead staining results were consistent with the number of bacterial colonies. To further investigate the reliability of the bactericidal effect, the integrity of the bacterial morphology of *S. aureus* and *E. coli* under the PMCL + laser treatment was detected by SEM. The SEM results showed that the cell membrane of the bacteria (*S. aureus* and *E. coli*) remained intact and smooth in the PBS group, showing a grape-like shape and a rod-like shape, respectively. After treatment with PMCL + laser, the bacteria were rough, wrinkled, and even broken on the surface, and the contents leaked out, suggesting that the bacterial membrane system was disrupted (Fig. 7B). These results confirmed that the PMCL nanozymes exhibited an antibacterial effect during the synergistic chemo-photodynamic therapy.

3.7. Cytotoxicity of the PMCL nanozymes

The potential virulence of antibacterial materials is a crucial issue in biomedical applications. The cell toxicity of PMCL in the L929 cells was first evaluated by MTT assays. As shown in Fig. 8A, negligible cytotoxicity was identified after the treatments of PL, PCL, PML and PMCL. The cell viabilities exceeded 90% even as the concentration reached 30 μg mL^{-1}. Additionally, the phototoxicity was also evaluated (Fig. 8B). Under 671 nm laser irradiation, the cell viabilities were approximately 93% after the treatment of PL. For the PCL and PML groups, the cell survival rates were approximately 89% and 90%, respectively. For the PMCL group, the cell viability of L929 fibroblasts under laser irradiation was above 88%, indicating the insignificant cytotoxicity.

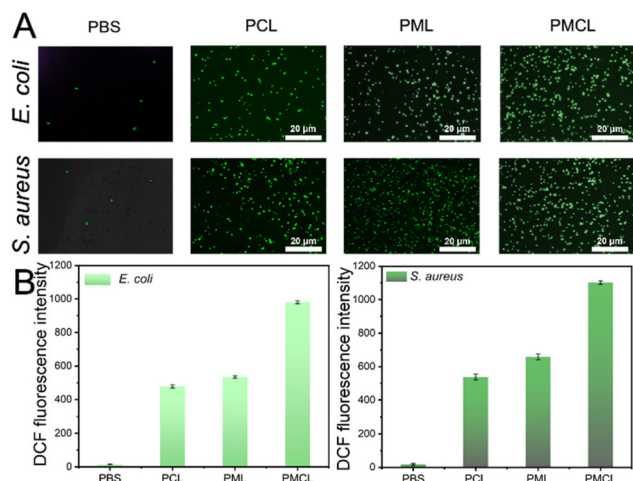### 3.8. ROS generation of PMCL in bacteria

The ROS generation in the bacterial suspension was investigated using DCFH-DA as an indicator. DCFH-DA can react with ROS to produce fluorescent dichlorofluorescein (DCF). The fluorescence intensity of DCF is positively related to the ROS generation level (Fig. 9A). For the PML + laser group, the green fluorescence intensity of DCF corresponds to the $^{\bullet}OH$ content. For the PCL + laser group, the green fluorescence intensity is consistent with the $^{1}O_2$ content. For the PMCL + laser group, MnO_2 catalyzes the decomposition of endogenous H_2O_2 to generate O_2, thereby increasing the content of $^{1}O_2$. Meanwhile, H_2O_2 is catalyzed to produce $^{\bullet}OH$. Both ROS ($^{1}O_2$ and $^{\bullet}OH$) can oxidize DCFH-DA to exhibit a green fluorescence signal. Therefore, the fluorescence signal for the PMCL group was significantly higher than the other groups. As shown in Fig. 9B, ROS generation was recorded by DCFH-DA staining
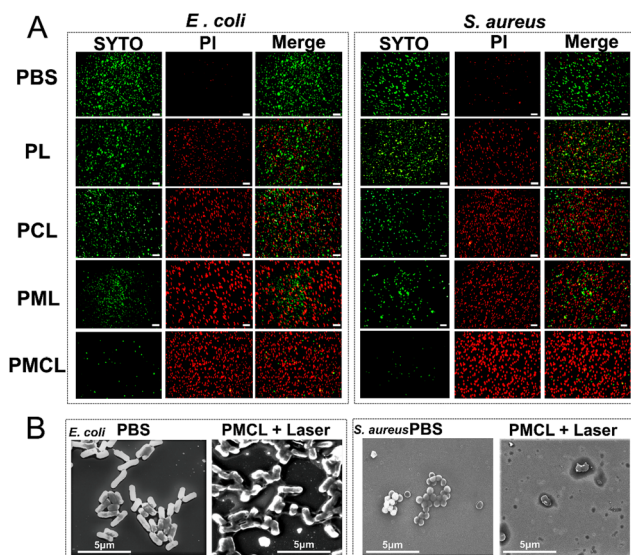
Fig. 7 (A) Live/dead fluorescence staining of *S. aureus* and *E. coli* after the laser irradiation treatment. Green fluorescence indicates live bacteria; red fluorescence indicates dead bacteria (scale bar: 40 μm). (B) SEM images of *E. coli* and *S. aureus* after different treatments (PBS and PMCL + laser group) (scale bar: 5 μm).
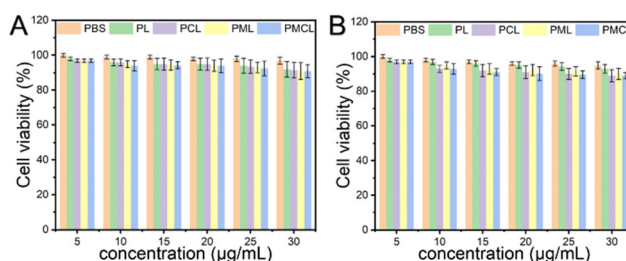
Fig. 8 *In vitro* cell cytotoxicity assay. Cell viability of L929 cells after being incubated with PBS, PL, PCL, PML and PMCL without (A) or with (B) laser irradiation.
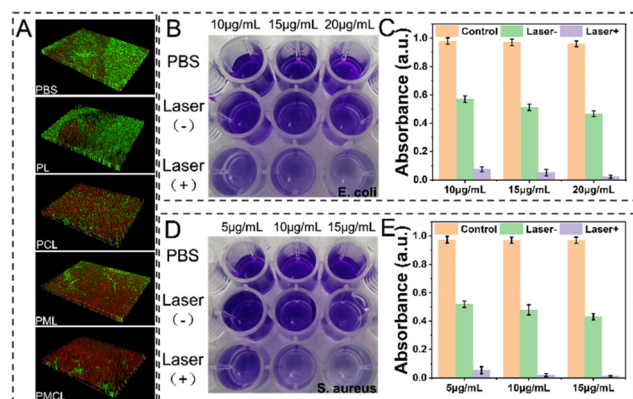
Fig. 9 (A) Detection of intracellular ROS by DCFH-DA staining bacteria incubated with PML, PCL and PMCL (scale bar: 100 μm). (B) Quantification of ROS generation ($\lambda_{excitation}$ = 485 nm and $\lambda_{emission}$ = 528 nm).

using a Polarstar microplate reader. For the PCL + laser group, the ROS intensity of *E. coli* and *S. aureus* was significantly increased to 478 ± 5.8 and 538 ± 6.3 compared to the untreated control samples. For the PML + laser group, the DCF green fluorescence intensity of *E. coli* and *S. aureus* was due to the increased ·OH content, reaching 524 ± 7.4 and 568 ± 4.6, respectively. After the PMCL + laser treatment, the highest green fluorescence was observed within *E. coli* and *S. aureus* based on the synergistic effect. The DCF fluorescence intensity reached 1181 ± 6.1 and 1403 ± 5.7, respectively. This phenomenon can be attributed to the PMCL having a strong ability to generate multiple ROS in bacteria through photodynamic and chemodynamic processes.
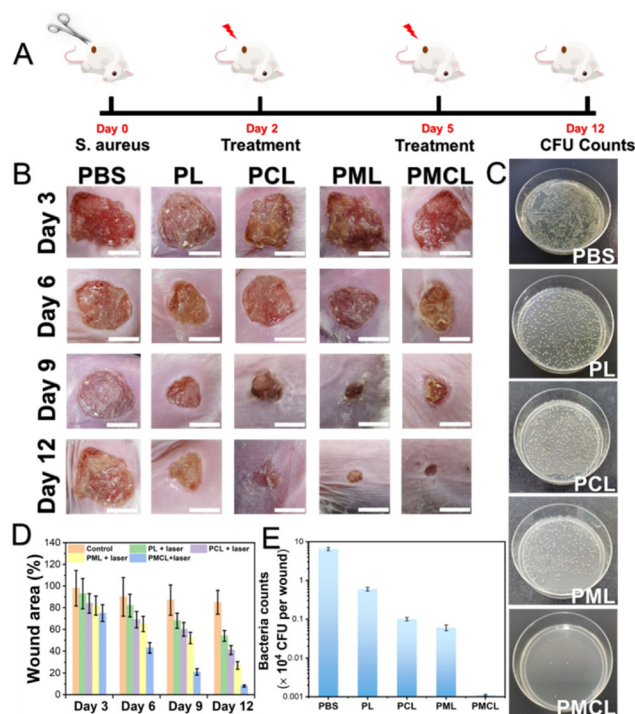
3.9. Eradication of bacterial biofilms

Chronic wound infections are regularly associated with the formation of bacterial biofilms.[35] The biofilm eradication capa-

Fig. 10 (A) CLSM images of the *S. aureus* biofilms after treatment with PBS, PL, PCL, PML, and PMCL with laser irradiation. Images of (B) *E. coli* and (D) *S. aureus* biofilms (stained by the Crystal Violet assay) after treatment with different PMCL concentrations. The survival rate of pre-formed (C) *E. coli* and (E) *S. aureus* biofilms after treatment with PMCL.

bility of PMCL was evaluated by the live/dead staining assay. Fig. 10A shows the 3D fluorescence images of the *S. aureus* biofilms after the treatment with PBS, PL, PML, PCL and PMCL, respectively. The biofilms in the PBS group were very dense and emitted strong green fluorescence. Trace amounts of dead bacteria (red fluorescence) were observed for the PL + laser group, suggesting that only a small part of the bacterial biofilms was damaged by hyperthermia. Notably, stronger red fluorescence signals were detected for the PML and PCL groups, indicating that the CDT and PDT can effectively destroy the structure of the bacterial biofilms, respectively. For the PMCL + laser group, the brightest red fluorescence was observed, suggesting that synergistic chemo-photodynamic therapy destroys the bacterial biofilms completely. Crystal violet staining assay was further performed to assess the synergy of PDT and CDT in eradicating biofilms. As shown in Fig. 10B and C, approximately 95% of the *E. coli* biofilms were removed after the treatment with PMCL (20 μg mL^{-1}) under laser irradiation (671 nm, 0.48 W cm^{-2}). The eradication capacity of *S. aureus* biofilms was similar to that of *E. coli* (Fig. 10D and E). These results suggest that efficient generation of dual-modal ROS can eliminate biofilms.

Fig. 11 Therapeutic efficacy of PMCL + laser in the *in vivo* wound treatment. (A) Schematic illustration for the establishment of the wound model, the treatment and the evaluation of the treatment effects. (B) Images of the infected skin wounds treated with the PBS, PL, PCL, PML, and PMCL at different time points (0, 1, 3 and 7 days) in the absence or presence of 671 nm laser irradiation (scale bar: 5 mm). (C) Plate images of the bacterial amount in skin wound at day 12. (D) The results of bacterial counting at wounds after treatment with different samples. (E) Quantitative assessment of bacterial counts after different treatments.

3.10. Antibacterial and wound-healing abilities in an animal model

A wound model infected with *S. aureus* was established to evaluate the antibacterial efficacy *in vivo* (Fig. 11A). All the mice with *S. aureus*-infected wounds were randomly divided into five groups and treated with PBS, PL, PCL, PML, and PMCL under laser irradiation. The initial day was considered as day 0 and the wound area was photographed every 3 days. After the 12th day, the PMCL + laser group showed the most significant healing effect on the wound infections. The wound was the smallest among all the experimental groups (Fig. 11B). As shown in Fig. 11C, after the 12-day treatment, the relative wound area was larger than 5% in the (I) PBS group, (II) PL group, (III) PCL group, and (IV) PML group. However, the relative wound area in the (V) PMCL group (2.93%) was significantly lower compared to the above four treatment groups. Furthermore, to verify the therapeutic effect quantitatively, the bacteria from the infection sites were evaluated using the agar plate dilution method (Fig. 11D). As shown in Fig. 11E, there was almost no living *S. aureus* in the PMCL + laser treated groups. According to the quantitative analysis, there was a large number of surviving *S. aureus* in the PBS + NIR treated wounds (8.86×10^4) The results suggested that PMCL showed a conspicuous bactericidal effect with the fewest bacteria colonies, which was ascribed to the generation of dual-modal ROS by the chemo-photodynamic effect at the wound sites.

4. Conclusions

In summary, a dual-modal ROS generator based on multi-functional PMCL nanozymes has been successfully synthesized for synergistic chemo-photodynamic antibacterial therapy. PMCL nanozymes adhere to bacteria by liposome–membrane fusion. MnO_2 promotes the conversion of endogenous H_2O_2 to $^{\bullet}OH$. Meanwhile, MnO_2 catalyzes H_2O_2 to generate O_2, enhancing the PDT efficiency. Furthermore, the photothermal effect further accelerates the generation of ROS. Thus, PMCL nanozymes achieve chemo-photo-dynamic synergistic antibacterial therapy through dual-modal ROS generation simultaneously. The biofilm eradication rates of PMCL against *E. coli* and *S. aureus* are 99.47% and 99.76%, respectively. Furthermore, the PMCL nanozymes are used to treat the mouse wound model of *S. aureus* infection. Overall, the multiple ROS antibacterial generator of synergistic chemo-photodynamic therapy can lead to powerful antibacterial efficacy. Our work may open up a new avenue for the exploration of efficient synergistic antibacterial therapy.

Conflicts of interest

There are no conflicts to declare.

Acknowledgements

References

1 S. Q. An, J. Murtagh, K. B. Twomey, M. K. Gupta, T. P. O'Sullivan, R. Ingram, M. A. Valvano and J. L. Tang, *Nat. Commun.*, 2019, **10**, 2334.

2 W. Ma, Z. Pang, X. Huang, J. Xu, S. S. Pandey, J. Li, D. S. Achor, F. N. C. Vasconcelos, C. Hendrich, Y. Huang, W. Wang, D. Lee, D. Stanton and N. Wang, *Nat. Commun.*, 2022, **13**, 529.

3 J. Larsen, C. L. Raisen, X. Ba, N. J. Sadgrove, G. F. Padilla-Gonzalez, M. S. J. Simmonds, I. Loncaric, H. Kerschner, P. Apfalter, R. Hartl, A. Deplano, S. Vandendriessche, B. Cerna Bolfikova, P. Hulva, M. C. Arendrup, R. K. Hare, C. Barnadas, M. Stegger, R. N. Sieber, R. L. Skov, A. Petersen, O. Angen, S. L. Rasmussen, C. Espinosa-Gongora, F. M. Aarestrup, L. J. Lindholm, S. M. Nykasenoja, F. Laurent, K. Becker, B. Walther, C. Kehrenberg, C. Cuny, F. Layer, G. Werner, W. Witte, I. Stamm, P. Moroni, H. J. Jorgensen, H. de Lencastre, E. Cercenado, F. Garcia-Garrote, S. Borjesson, S. Haeggman, V. Perreten, C. J. Teale, A. S. Waller, B. Pichon, M. D. Curran, M. J. Ellington, J. J. Welch, S. J. Peacock, D. J. Seilly, F. J. E. Morgan, J. Parkhill, N. F. Hadjirin, J. A. Lindsay, M. T. G. Holden, G. F. Edwards, G. Foster, G. K. Paterson, X. Didelot, M. A. Holmes, E. M. Harrison and A. R. Larsen, *Nature*, 2022, **602**, 135.

4 Q. Jia, Q. Song, P. Li and W. Huang, *Adv. Healthcare Mater.*, 2019, **8**, e1900608.

5 B. Tse Sum Bui, T. Auroy and K. Haupt, *Angew. Chem., Int. Ed.*, 2022, **61**, e202106493.

6 S. Wu, C. Xu, Y. Zhu, L. Zheng, L. Zhang, Y. Hu, B. Yu, Y. Wang and F. J. Xu, *Adv. Funct. Mater.*, 2021, **31**, 2103591.

7 Z. Liu, X. Zhao, B. Yu, N. Zhao, C. Zhang and F. J. Xu, *ACS Nano*, 2021, **15**, 7482.

8 J. X. Fan, M. Y. Peng, H. Wang, H. R. Zheng, Z. L. Liu, C. X. Li, X. N. Wang, X. H. Liu, S. X. Cheng and X. Z. Zhang, *Adv. Mater.*, 2019, **31**, e1808278.

9 H. Zhang, Y. Zhu, Y. Li, X. Qi, J. Yang, H. Qi, Q. Li, Y. Ma, Y. Zhang, X. Zhang and L. Zhang, *Adv. Funct. Mater.*, 2021, **31**, 2104799.

10 D. Zhuge, L. Li, H. Wang, X. Yang, D. Tian, Q. Yin, H. Chen, C. Weng, B. Wen, Y. Lin, J. Y. Huh, X. Zhang, M. Chen, C. Xie, Y. Zhao and Y. Chen, *Adv. Healthcare Mater.*, 2022, **11**, e2200698.

11 T. Zhou, R. Hu, L. Wang, Y. Qiu, G. Zhang, Q. Deng, H. Zhang, P. Yin, B. Situ, C. Zhan, A. Qin and B. Z. Tang, *Angew. Chem., Int. Ed.*, 2020, **59**, 9952.

12 F. Gao, T. Shao, Y. Yu, Y. Xiong and L. Yang, *Nat. Commun.*, 2021, **12**, 745.

13 X. Zhang, G. Li, G. Chen, D. Wu, Y. Wu and T. D. James, *Adv. Funct. Mater.*, 2021, **31**, 2106139.

14 Z. Zhu, L. Wang, Y. Peng, X. Chu, L. Zhou, Y. Jin, H. Guo, Q. Gao, J. Yang, X. Wang, Z. Long, Y. Ge, S. Lu and B. Wang, *Adv. Funct. Mater.*, 2022, **32**, 2201875.

15 D. Cui, J. Huang, X. Zhen, J. Li, Y. Jiang and K. Pu, *Angew. Chem., Int. Ed.*, 2019, **58**, 5920.

16 X. Wang, Q. Shi, Z. Zha, D. Zhu, L. Zheng, L. Shi, X. Wei, L. Lian, K. Wu and L. Cheng, *Bioact. Mater.*, 2021, **6**, 4389.

17 L. Zhang, Z. Liu, Q. Deng, Y. Sang, K. Dong, J. Ren and X. Qu, *Angew. Chem., Int. Ed.*, 2021, **60**, 3469.

18 A. Eskenazi, C. Lood, J. Wubbolts, M. Hites, N. Balarjishvili, L. Leshkasheli, L. Askilashvili, L. Kvachadze, V. van Noort, J. Wagemans, M. Jayankura, N. Chanishvili, M. de Boer, P. Nibbering, M. Kutateladze, R. Lavigne, M. Merabishvili and J. P. Pirnay, *Nat. Commun.*, 2022, **13**, 302.

19 K. Guo, M. Zhang, J. Cai, Z. Ma, Z. Fang, H. Zhou, J. Chen, M. Gao and L. Wang, *Small*, 2022, **18**, e2108030.

20 X. Hu, H. Zhang, Y. Wang, B.-C. Shiu, J.-H. Lin, S. Zhang, C.-W. Lou and T.-T. Li, *Chem. Eng. J.*, 2022, **450**, 138129.

21 Y. Zhu, D. Jin, M. Liu, Y. Dai, L. Li, X. Zheng, L. Wang, A. Shen, J. Yu, S. Wu, Y. Wu, K. Zhong, J. Cheng and Y. Liu, *Small*, 2022, **18**, e2200116.

22 P. Zhang, Q. Wu, J. Yang, M. Hou, B. Zheng, J. Xu, Y. Chai, L. Xiong and C. Zhang, *Acta Biomater.*, 2022, **146**, 450.

23 S. Guan, X. Liu, C. Li, X. Wang, D. Cao, J. Wang, L. Lin, J. Lu, G. Deng and J. Hu, *Small*, 2022, **18**, e2107160.

24 Y. Shi, L. Zeng, Y. Pan, H. Zhang, Z. Wang, Y. Shi and A. Wu, *Acta Biomater.*, 2022, **10**, 1742.

25 X. Zhao, K. Guo, K. Zhang, S. Duan, M. Chen, N. Zhao and F. J. Xu, *Adv. Mater.*, 2022, **34**, e2108263.

26 X. Qi, Y. Huang, S. You, Y. Xiang, E. Cai, R. Mao, W. Pan, X. Tong, W. Dong, F. Ye and J. Shen, *Adv. Sci.*, 2022, **9**, e2106015.

27 W. Chen, H. Miao, G. Meng, K. Huang, L. Kong, Z. Lin, X. Wang, X. Li, J. Li, X. Y. Liu and N. Lin, *Small*, 2022, **18**, e2107196.

28 J. Fang, Y. Wan, Y. Sun, X. Sun, M. Qi, S. Cheng, C. Li, Y. Zhou, L. Xu, B. Dong and L. Wang, *Chem. Eng. J.*, 2022, **435**, 134935.

29 S. Wenjie, A. Jinxia, T. He, J. Mengran and G. Hui, *Adv. Healthcare Mater.*, 2022, **11**, e2101633.

30 F. Li, K. Huang, H. Chang, Y. Liang, J. Zhao, S. Yang and F. Liu, *Acta Biomater.*, 2022, **150**, 380.

31 X. Han, Q. Lou, F. Feng, G. Xu, S. Hong, L. Yao, S. Qin, D. Wu, X. Ouyang, Z. Zhang and X. Wang, *Angew. Chem., Int. Ed.*, 2022, **61**, e202202559.

32 M. Li, L. Li, K. Su, X. Liu, T. Zhang, Y. Liang, D. Jing, X. Yang, D. Zheng, Z. Cui, Z. Li, S. Zhu, K. W. K. Yeung, Y. Zheng, X. Wang and S. Wu, *Adv. Sci.*, 2019, **6**, 1900599.

33 Y. Zhao, X. Dai, X. Wei, Y. Yu, X. Chen, X. Zhang and C. Li, *ACS Appl. Mater. Interfaces*, 2018, **10**, 14426.

34 J. Xie, Z. Meng, X. Han, S. Li, X. Ma, X. Chen, Y. Liang, X. Deng, K. Xia, Y. Zhang, H. Zhu and T. Fu, *Adv. Healthcare Mater.*, 2022, **11**, e2101745.

35 S. Darvishi, S. Tavakoli, M. Kharaziha, H. H. Girault, C. F. Kaminski and I. Mela, *Angew. Chem., Int. Ed.*, 2022, **61**, e202112218.